Bubble Rise In An Inclined Channel

Murray J. Rudman and Hugh M. Blackburn
Advanced Fluid Dynamics Laboratory
Division of Building, Construction and Engineering
Commonwealth Scientific and Industrial Research Organisation (CSIRO)
P.O. Box 56, Highett, Victoria 3190

Justin Merrell
Comalco Research Centre
P.O. Box 316, Thomastown, Victoria 3074

ABSTRACT

The rise of two-dimensional bubbles in an inclined channel is studied numerically. The numerical scheme uses a conservative finite-difference formulation that solves the equations of motion for both liquid and gas phases. Accurate calculation of the interface position and interfacial forces between gas and liquid are an essential part of the numerical scheme. Careful attention is also paid to mass and momentum advection, and robust and reliable convergence of the pressure field depends heavily on a multigrid technique. Bubble shape and rise velocity are found to be strongly dependent on the relative size of the bubble and channel height and less strongly dependent on inclination angle and coefficients of viscosity and surface tension.

NOMENCLATURE

A Bubble cross sectional area

C Volume fraction of phase 1

$\hat{\boldsymbol{g}}$ Gravity unit vector

$\boldsymbol{F}_S$ Interfacial force

Fr Froude number

$\mathcal{L}$ Channel height

P Pressure

R' Equivalent bubble radius

Re Reynolds number

t Time

$\boldsymbol{U}$ Velocity vector

$\mathcal{U}$ Velocity scale

We Weber number

δt Time-step

δP Pressure correction

μ Dynamic viscosity

ρ Density

τ Viscous stress tensor

1. INTRODUCTION

The motion of large gas bubbles plays a key role in many industrial processes, and applications include gas sparging, pipeline hold-up due to slugs, boiling heat transfer under downward-facing heating surfaces and bubbling in electrolytic cells. A good understanding of the physics of bubble rise is essential, as bubble motion affects heat transfer in boiling processes and voltage drop in electrolytic applications. The present study is motivated by the need to estimate bubble rise velocities and understand fluid flow patterns in an inclined channel geometry that modelled an anode-cathode gap in a reduction cell. Geometries such as this occur in

bi-polar battery cells and Hall-Heroult cells used widely in the production of aluminium.

Experimental studies of the rise of gas bubbles underneath an inclined plane have been published by Maneri & Zuber (1974); Che, Chen & Taylor (1991); and Maxworthy (1991), however the literature is sparse. The two-dimensional bubbles considered here may be thought of as a prototype for more realistic three-dimensional flows and more complex geometries such as those for bubble rise in inclined pipes.

Numerical simulation of the motion of large, discrete gas bubbles through a liquid is difficult, since the interface position is unknown and thus becomes an additional variable in the problem formulation. Added to this difficulty is the numerical stiffness that results from large differences in density between gas and liquid (typically three orders of magnitude). Interfacial forces between gas and liquid are essential in predicting bubble shape and rise velocity, and because these forces are restricted to the interface (which has one less dimension than the flow solution space) their accurate prediction introduces special difficulties to the numerical solution of the problem.

2. NUMERICAL METHOD

Liquid and gas are modelled as a single fluid with variable density and viscosity. The equations of motion for this system are written

$$\frac{\partial C}{\partial t} + \nabla\cdot(\boldsymbol{U}C) = 0, \tag{1}$$

$$\rho = \rho_1 C + \rho_2(1-C), \tag{2}$$

$$\begin{aligned}\frac{\partial \rho\boldsymbol{U}}{\partial t} &+ \nabla\cdot(\rho\boldsymbol{U}\boldsymbol{U}) \\ &= -\nabla P + \frac{1}{\mathrm{Fr}^2}\rho\hat{\boldsymbol{g}} + \frac{1}{\mathrm{We}}\boldsymbol{F}_S + \frac{1}{\mathrm{Re}}\nabla\cdot\tau\end{aligned} \tag{3}$$

$$\nabla\cdot\boldsymbol{U} = 0. \tag{4}$$

Instead of advecting density, a scalar indicator (or *phase* function) C is advected with the local velocity $\boldsymbol{U}$. The density (and other scalar quantities such as viscosity) are obtained as shown in 2.

The dimensionless parameters in 1–4 are

$$Re = \frac{\rho_0\mathcal{U}\mathcal{L}}{\mu_0}, \quad We = \frac{\rho\mathcal{U}^2\mathcal{L}}{\sigma}, \quad Fr = \frac{\mathcal{U}}{\sqrt{g\mathcal{L}}},$$

where $\mathcal{U}$ is an (unknown) velocity scale, $\mathcal{L}$ is the channel height, and ρ_0 and μ_0 are the liquid density and viscosity. The coefficient of surface tension is σ and g is the gravitational acceleration. In all simulations described below, the velocity scale is chosen to be $\mathcal{U} = \sqrt{g\mathcal{L}}$ which is equivalent to $\mathrm{Fr} \equiv 1$.

A basic first-order temporal integration algorithm is:

1. Estimate values of C by solving

$$C^{n+1} = C^n - \delta t\nabla\cdot(C^n\boldsymbol{U}^n),$$

and estimate densities and viscosities from

$$\begin{aligned}\rho^{n+1} &= \rho_g C^{n+1} + \rho_f(1-C^{n+1}),\\ \mu^{n+1} &= \mu_g C^{n+1} + \mu_f(1-C^{n+1}).\end{aligned}$$

2. Find intermediate values of the velocity field by solving

$$\begin{aligned}\boldsymbol{U}^* = \frac{\rho^n\boldsymbol{U}^n}{\rho^{n+1}} + \frac{\delta t}{\rho^{n+1}}\big[&-\mathcal{A}(\boldsymbol{U}^n) - \nabla P^n \\ &+ \mathcal{D}(\mu^n, \boldsymbol{U}^n)\big],\end{aligned}$$

where the symbols $\mathcal{A}$ and $\mathcal{D}$ refer to the advective and diffusive operators respectively.

3. Calculate the pressure correction, δP, from the discrete form of the following Helmholtz equation

$$\nabla\cdot\left(\frac{1}{\rho^{n+1}}\nabla\delta P\right) = \frac{1}{\delta t}\nabla\cdot\boldsymbol{U}^*.$$

4. Update velocity and pressure

$$\begin{aligned}\boldsymbol{U}^{n+1} &= \boldsymbol{U}^* - \frac{\delta t}{\rho^{n+1}}\nabla\delta P,\\ P^{n+1} &= P^n + \delta P.\end{aligned}$$

Time evolution is accomplished using an explicit, second-order, improved Euler scheme which involves repetition of the steps above, once with a half time-step, and then once with a full time-step with the right-hand side of each equation (except 1) determined using half-time estimates of $\boldsymbol{U}$, ρ and P.

Solution of the equations occurs on a uniform, staggered MAC mesh (Welch, Harlow, Shannon & Daly 1965). In this mesh system,

all scalar quantities (P, C, μ, etc.) are defined at cell centres, the x-component of velocity, U, is defined at right- and left-hand cell edges, and the y-component of velocity, V, is defined at the top and bottom cell edges.

In order to maintain sharp interfaces, special Volume-of-Fluid (VOF) techniques must be used to advect C. The method here is designed especially to ensure that mass and momentum advection are consistent. It is based on the piecewise linear interface construction method of Youngs (1982) and utilises a C-mesh that is twice as fine as that used for momentum and pressure (Rudman 1997).

Intermediate velocity calculation (step 2) is undertaken using a purely explicit estimate of the right hand sides. The pressure term is calculated using centred differences as is the viscous term. Because the viscosity is not constant, the viscous term must be written in stress-divergence form. Momentum advection utilises the fully multi-dimensional Flux-Corrected-Transport (FCT) method of Zalesak (1979). Low-order momentum fluxes are calculated using first order up-winding, and high-order fluxes use a third-order QUICK scheme. In both cases, up-wind estimates of velocities are used whereas cell-edge densities are estimated in a pseudo-characteristic manner, being determined on the basis of C-advection on the fine mesh. Limiting is almost identical to that in Zalesak except that the minimum and maximum values of velocity (not momentum) are used to ensure monotonicity. Details of the momentum advection algorithm are described in Rudman (1997).

The pressure correction solution (step 3) is based on the multigrid method of Wesseling (1992). In order to obtain robust and rapid convergence of the method, it is necessary to employ:

- zeroth-order interpolation for the prolongation operator [P];
- a 16-point stencil based on an average of linear interpolation in triangles and linear interpolation in lines for the restriction operator [R]; and
- the Galerkin coarse grid operator [Ã] discussed in Wesseling (1992), i.e. [Ã] = [R][A][P].

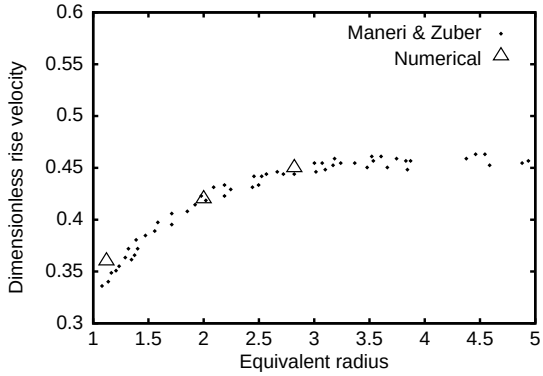

Figure 1: Dimensionless rise velocity as a function of equivalent bubble radius (cm). Comparison of numerical results with experiments of Maneri and Zuber (1974).

The convergence rate of this multigrid method is independent of the mesh size and weakly dependent on the density ratio of the problem, rising from the equivalent of approximately twenty-five fine grid iterations at a density ratio of 1:1, to fifty at a density ratio of 1000:1.

3. VALIDATION

Validation of the numerical model is undertaken here by comparing the numerical results to the experimental results of Maneri & Zuber (1974). In that study, gas bubbles were released in a sloping channel sandwiched between two vertical glass plates. The resulting flows can be considered two-dimensional. The experimental results at 10° inclination are compared to numerical results of rise velocity in Figure 1, which shows dimensionless rise velocity (non-dimensionalised by $\sqrt{g\mathcal{L}}$) versus equivalent bubble radius (the radius of the circle with equal cross-sectional area to the bubble). The agreement is seen to be good and, as observed experimentally, the bubble rise velocity decreases as the equivalent bubble radius decreases. Validation for bubbles with an equivalent radius larger than 3 cm is not feasible at the present time due to the very large computational domains required.

4. RESULTS

As the bubble rises, it is assumed that it induces an equal and opposite counter flow beneath it. Thus there is assumed to be no net pumping of fluid by bubble rise. In order to minimise the size of the computational domain, all simulations have been undertaken in a coordinate frame that moves approximately with the leading edge of the bubble. Because the rise velocity is not known a priori, the process of finding the correct rise velocity is an iterative one. Initial conditions are uniform inflow with a small bubble at the upper wall. Gas is blown into the bubble through the top boundary until the desired bubble size is attained. Once the bubble reaches the desired size, estimates of rise velocity and mean bubble shape are made. The simulations discussed here correspond to an air/water system with channel heights of 12, 30 and 48 mm and channel inclinations of 2° and 4° from the horizontal.

Bubble rise in this air/water system is an unsteady phenomenon as seen in Figure 2, which shows an instantaneous bubble profile and velocity vectors in the computational frame and in a stationary coordinate frame. Clearly seen in Figure 2(b) are vortices that have been shed from the rising bubble. Interaction of these bubbles with the interface ensures unsteadiness in the flow and sometimes leads to detachment of significant fractions of the bubble.

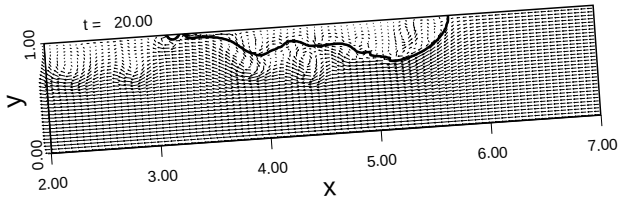

(a)

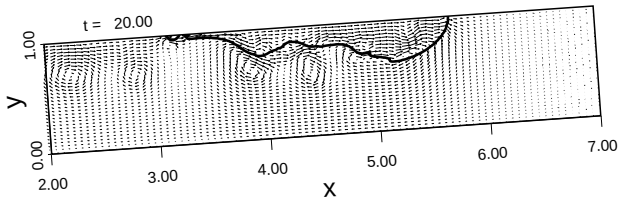

(b)

Figure 2: Instantaneous bubble shape and velocity vectors for bubble rise in a channel inclined at 4°: (a) Computational coordinate frame, (b) coordinate frame stationary with respect to the walls. Every fourth vector in each direction is displayed.

4.1 Time-mean bubble shape

Non-dimensional bubble size is quantified using a non-dimensional equivalent bubble radius

$$R' = \frac{1}{\mathcal{L}} \left(\frac{A}{\pi} \right)^{1/2},$$

where A is the cross-sectional area of the bubble and $\mathcal{L}$ is the channel height. The time-mean bubble shape is primarily a function of channel inclination and R'. The time-mean bubble shape for a range of non-dimensional bubble sizes is shown in Figure 3 for a channel inclination of 2° and Figure 4 for 4°. The time-mean bubble profile can be split into several pieces: (i) a round nose that is well represented with a circular arc, (ii) an almost straight edge that is absent in small bubbles and increases in length once the bubble fills approximately half the channel width, and (iii) a tail that is approximately horizontal. The radius of curvature of the bubble nose increases with increasing bubble size. A fourth feature that is often present, especially for larger bubble sizes, is

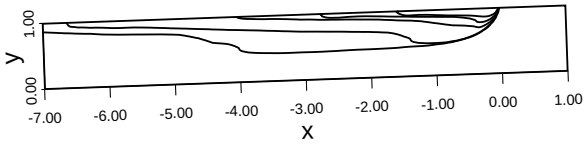

Figure 3: Time-mean bubble shapes for R' of 1.0, 0.7, 0.4, 0.28 and 0.2. Data are for a channel inclination of 2° and are taken from a range of channel heights.

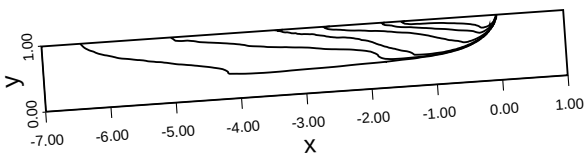

Figure 4: Time-mean bubble shapes for R' of 1.0, 0.7, 0.56, 0.4, 0.28 and 0.2. Data are for channel inclination of 4° and are taken from a range of channel heights.

a small cusp that joins the circular nose to the flat tail. It is at this point that the flow generally separates from the bubble surface, leading to the formation of wake vortices and unsteadiness behind the bubble.

Unsteadiness resulting from vortex shedding may be beneficial in cooling applications and may help to mix any thermal stratifications that arise in the system.

Note that as the channel inclination is increased, the bubbles become shorter and the blockage presented by the bubble increases for a given bubble size. Also, as the bubble size increases for a fixed inclination, the blockage presented by the bubble appears to asymptote to a constant value (different for each inclination).

4.2 Bubble rise velocity

Bubble rise velocities are estimated to lie in the range 0.10–0.25 m/s for the range of parameters considered here. The rise velocity, non-dimensionalised with $\sqrt{g\mathcal{L}}$, is plotted against R' in Figure 5. The data for 2° channel inclination consistently lie below those for 4°, which is not unexpected as the tangential component of the buoyancy force decreases with decreasing inclination. However, the difference in the rise velocity of small bubbles is proportionally greater than the differences for large bubbles. For the largest bubble size ($R' = 1.0$) the difference in rise velocity is negligible. The theoretical results of Couët & Strumulo (1987) suggest that for infinitely large bubbles, the non-dimensional rise velocity of two-dimensional bubbles asymptotes to a constant value as the channel inclination approaches 0°. (In the limiting case, bubble motion should be considered to be a gravity current and not a discrete bubble.) Thus the observation here that rise velocity becomes less sensitive to inclination angle for larger bubbles is not surprising. (Note that the asymptotic value as the inclination approaches zero is dependent on the magnitude of surface tension.)

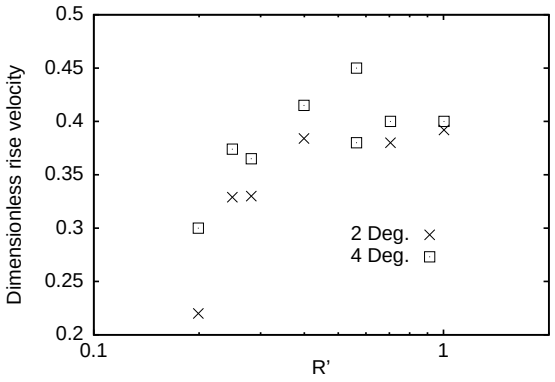

Figure 5: Non-dimensional bubble rise velocity (velocity divided by $(g\mathcal{L})^{1/2}$) versus non-dimensional bubble size, R'.

For a given angle, non-dimensional rise velocities do not fall on a single curve. This is a reflection of the role that surface tension plays in determining rise velocity. As the channel height decreases, surface tension forces become proportionally greater for the same R'. It is observed here that increasing surface tension decreases non-dimensional rise velocity for all bubble sizes, in line with the theoretical results of Couët & Strumulo (1987) which showed the same trend for infinitely large bubbles.

Although not clear from Figure 5, as R' increases bubble rise velocity asymptotes to a constant value for a fixed channel height. This is in agreement with the experimental results of Maneri & Zuber (1974) and is related to the blockage presented by the bubble, which also asymptotes as bubble size increases.

5. SUMMARY

A numerical method has been presented that allows the simulation of gas-liquid interfacial flows. Application of the method to study the rise of large two-dimensional gas bubbles in an inclined channel at low inclination angles has shown that bubble rise is highly unsteady and that vortices are shed from the bubble sides. The unsteadiness may have advantages in some systems by providing mixing and ensuring even temperature and chemical compositions. Bubble rise is also seen to be a complex function of bubble size, channel inclination and surface tension.

REFERENCES

Che, D. F., Chen, J. J. J. & Taylor, M. P. (1991). Gas bubble formation and rise velocity beneath a downward facing in-

clined surface submerged in a liquid, *Trans. IChemE* **69**: 25–29.

Couët, B. & Strumulo, G. S. (1987). The effects of surface tension and tube inclination on a two-dimensional rising bubble, *J. Fluid Mech.* **184**: 1–14.

Maneri, C. C. & Zuber, N. (1974). An experimental study of plane bubbles rising at inclination, *Int. J. Multiphase Flow* **1**: 623–645.

Maxworthy, T. (1991). Bubble rise under an inclined plate, *J. Fluid Mech.* **229**: 659–674.

Rudman, M. (1997). CSIRO-VOF: A VOF-based method for incompressible multi-fluid flows with large density variations, *Technical report*, CSIRO. Unpublished.

Welch, J. E., Harlow, F. H., Shannon, J. P. & Daly, B. J. (1965). The MAC method. a computing technique for solving viscous, incompressible, transient fluid-flow problems involving free surfaces, *Technical Report LA-3425*, Los Alamos Scientific Laboratory, Los Alamos, NM.

Wesseling, P. (1992). *An introduction to multigrid methods*, John Wiley and Sons, Chichester U.K.

Youngs, D. L. (1982). Time-dependent multi-material flow with large fluid distortion, *in* K. W. Morton & M. J. Baines (eds), *Numerical methods for fluid dynamics*, Academic press, New York, pp. 273–285.

Zalesak, S. T. (1979). Fully multi-dimensional flux corrected transport algorithms for fluid flow, *J. Comput. Phys.* **31**: 335–362.